The electrode-electrolyte interface in CO2 reduction and H2 evolution: a multiscale approach

Cecilio de Oliveira Monteiro, M

8

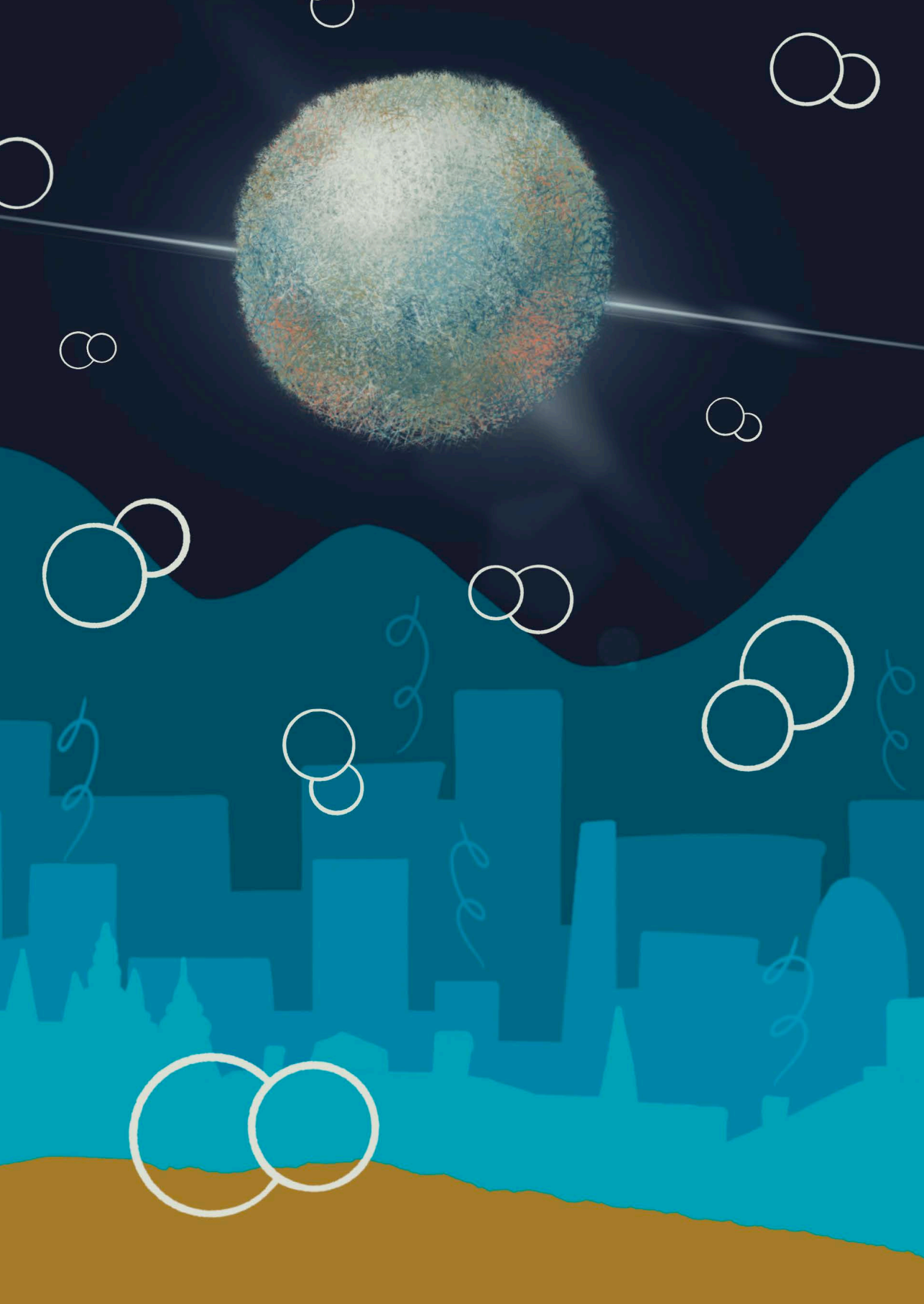# Absence of CO_2 electroreduction on copper, gold and silver electrodes without metal cations in solution

Abstract

The electrocatalytic reduction of carbon dioxide is widely studied for the sustainable production of fuels and chemicals. Metal ions in the electrolyte influence reaction performance, although their main role is under discussion. Here, we have studied CO_2 reduction on gold electrodes through cyclic voltammetry showing that without a metal cation the reaction does not take place in a pure 1 mM H_2SO_4 electrolyte. We have further investigated CO_2 reduction with and without metal cations in solution using Scanning Electrochemical Microscopy in the surface-generation tip-collection mode with a platinum ultramicroelectrode as a CO and H_2 sensor. CO is only produced on gold, silver or copper if a metal cation is added to the electrolyte. Density Functional Theory simulations confirmed that partially desolvated metal cations stabilize the CO_2^- intermediate *via* a short-range electrostatic interaction, enabling its reduction. Overall, our results redefine the reaction mechanism, providing definitive evidence that positively charged species from the electrolyte are key to stabilize the crucial reaction intermediate.

8.1 Introduction

The electrochemical carbon dioxide reduction reaction (CO_2RR) into fuels and chemicals has recently gained significant attention as a way to close the chemical carbon cycle and to store excess renewable electricity in fuels and chemicals. Good activity and selectivity of the CO_2RR are crucial to make the process industrially viable. In aqueous media, CO_2 reduction on metals such as gold and silver yields almost exclusively carbon monoxide (in addition to hydrogen from the competing proton/water reduction), while on copper C-C bonds are formed.[1] Tailoring the catalyst surface is the most common way of steering activity and selectivity. However, it is well known that the electrolyte composition, especially pH and cation, has a strong impact on the reaction.[2–4] To date, in the majority of the studies, alkali metals have been employed and the activity trend found on different electrodes is $Cs^+ > K^+ > Na^+ > Li^+$.[5–13] Even though this trend is consistent in different research works, diverging theories have been proposed to explain through which molecular mechanism cations affect CO_2 reduction.

There are three main theories which explain how cations at the interface affect the activity and selectivity of electrocatalytic processes, as recently reviewed by Waegele et. al.[14]: modification of the local electric field, buffering of the interfacial pH or stabilization of reaction intermediates. On a negatively charged metal electrode, there is still no agreement if cations adsorb specifically, or if their interaction with the surface is purely electrostatic.[15–17] Especially concerning CO_2RR, Hori and Murata presented one of the first explanations on how metal cations affect the reaction.[18,19] Based on Frumkin`s theory[20], they proposed that cations change the potential profile in the electric double layer through specific adsorption. Weakly hydrated cations lead to steeper potential gradients from the electrode surface towards the outer Helmholtz plane (OHP) compared to strongly hydrated species. More recent studies have ruled out specific adsorption and instead suggested that under CO_2RR conditions cations accumulate near the surface *via* non-covalent interactions giving rise to high electric fields in the vicinity of the ion.[21–23] For instance, Ringe et al. employed a continuum electrolyte model to show that weakly hydrated cations are more concentrated at the OHP and thus induce a higher mean electronic surface charge density, which in turn leads to an enhanced CO_2RR activity and selectivity.[21] A modification of the potential across the plane where the electron transfer happens is proposed to change the apparent activation energy of the

8

overall reaction, affect the interfacial water energetics, and influence CO_2 adsorption.

In contrast to the Frumkin-type local electric field effect, the second theory was put forward by Singh et al.[24] proposing that cations affect the CO_2RR by buffering the interfacial pH. Even though alkali cations do not undergo hydrolysis in the bulk, near the negatively charged cathode surface the hydration shell of large cations will experience a stronger electrostatic field, which decreases their pK_a of hydrolysis. Ayemoba and Cuesta[25] probed the pH at a gold-electrolyte interface using Attenuated Total Reflection Surface Enhanced Infra-Red Spectroscopy (ATR-SEIRAS) and based on the ratio between the integrated intensity of the CO_2 and HCO_3^- bands, the authors show that larger cations are better buffers and lead to lower pH changes at the interface. Zhang et al.[26] performed similar pH measurements using a Rotating-Ring-Disc Electrode (RRDE) and found that during CO_2 reduction in bicarbonate electrolyte the interfacial pH follows the trend: $Li^+ > Na^+ > K^+ > Cs^+$.

The third theory, introduced by Chen et al.[22] and further developed in the work of Resasco et al.[27], suggests that metal cations stabilize certain CO_2 reduction reaction intermediates through local electrostatic interactions within the electrical double layer. Specifically, the study of Resasco *et al.*[27] focused on the effect of alkali cations on CO_2 reduction over Cu(100) and Cu(111) thin-film electrodes and Ag and Sn polycrystalline electrodes. The formation of CO was suggested to happen through the reaction intermediates shown in Eq. 8.1-8.3:[1]

$$CO_2 + e^- + * \rightarrow *CO_2^- \qquad\qquad \text{Eq. 8.1}$$
$$*CO_2^- + H^+ \rightarrow *CO_2H \qquad\qquad \text{Eq. 8.2}$$
$$*CO_2H + H^+ + e^- \rightarrow *CO + H_2O \qquad\qquad \text{Eq. 8.3}$$

The selectivity trends reported in Ref. 27 are explained through Density Functional Theory (DFT) simulations on a surface/solvated cation interface optimized *via* constrained minima hopping molecular dynamics. Solvated cations with larger ionic radius experience a stronger driving force to accumulate near the surface.[27] As previously demonstrated by Chen et al.,[22] high local electrostatic fields generated by solvated cations can locally stabilize adsorbed intermediates with large dipole moments. Thus, the higher activity observed for CO_2 reduction on copper in the presence of larger cations was attributed to a higher concentration of such cations in the OHP.[27]

To test the above models, in this Chapter, we carry out CO_2 reduction experiments on polycrystalline gold, which is a stable and simple electrocatalytic

system that, under the conditions of this study, yields only CO and H$_2$. Measurements are performed in the total absence of metal cations (at pH = 3) and in the presence of small amounts of Cs$^+$. Using Scanning Electrochemical Microscopy in the surface-generation tip-collection mode (SG-TC) as an extremely sensitive technique to detect CO$_2$ reduction products, we show that without a metal cation in solution, CO$_2$ reduction does not take place. This remarkable observation is extended to other common catalysts like copper and silver. Of the three models existing in literature, only the model which considers electrostatic interactions between metal cations and key intermediates can explain this observation. We further confirm the role of cations through DFT-based *ab initio* molecular dynamics (AIMD) simulations on a gold/cation/solvent system where we prove the stabilization effect of partially desolvated metal cations on CO$_2$ adsorption, activation and formation of the CO$_2^-$ intermediate. While our results, in principle, do not exclude the validity of the other two models, they nonetheless clearly show that the main role of the metal cation is to stabilize the key CO$_2^-$ intermediate, to the extent that in its absence, CO$_2$ reduction does not take place. This conclusion has important implications for CO$_2$RR modeling and catalyst design.

8.2   Hanging meniscus experiments

In order to elucidate the role of metal cations in the CO$_2$RR, the reaction was first studied through cyclic voltammetry (CV) using a gold electrode in hanging meniscus configuration. On gold, under the conditions of this study, CO$_2$ is reduced in the cathodic scan producing only CO. The competing hydrogen evolution reaction (HER) occurs due to the reduction of protons or water, depending on the interfacial proton concentration. As gold is also a very good catalyst for CO oxidation, the CO produced can be probed semi-quantitatively by directly cycling the electrode to positive potentials. The gold electrode used in this study was characterized by blank voltammetry before each measurement (Fig. E.1 in Appendix E), in order to assure cleanliness of the surface, comparability and reproducibility of the experiments, and to allow the determination of the electrochemically active surface area. This consecutive cathodic/anodic cycling was performed first in argon and subsequently in CO$_2$ atmosphere.

Fig. 8.1a compares the cathodic scans obtained in the absence of a metal cation (in 1 mM H$_2$SO$_4$) and in the presence of 280 µM of Cs$^+$, both solutions at bulk pH = 3. Note that an experiment in the absence of metal cations (which is the focus
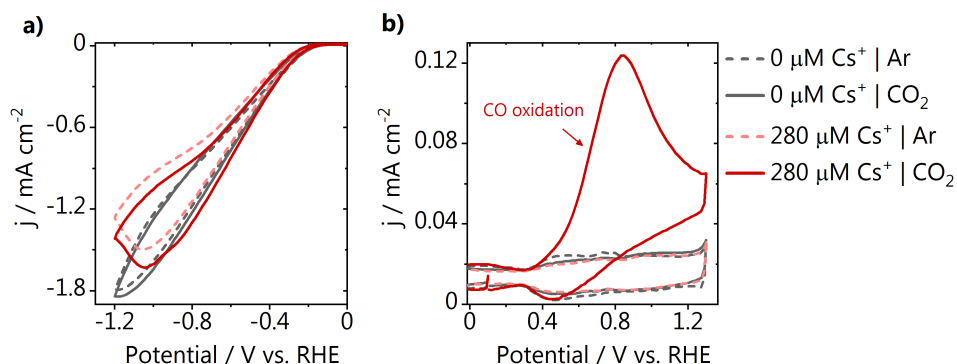
Fig. 8.1. CO_2 reduction on gold with and without 280 µM Cs^+ in solution. **a)** Cathodic scans recorded in argon and CO_2 atmosphere together with **b)** the subsequent recorded anodic scans performed to oxidize any CO produced. All CVs were recorded at 50 mV s^{-1}.

of this work) can only be performed at this or at a lower pH, as for a higher pH without metal cations the electrolyte conductivity would become prohibitively small. Still, due to the local production/consumption of OH^-/H^+, the alkalinity at the interface increases during the course of the reaction. In argon, when only hydrogen evolution is taking place, the proton reduction current is lower and reaches diffusion limitation at lower overpotentials in the presence of Cs^+. This is likely due to migration, which with Cs^+ in solution leads to a lower concentration of protons near the surface. This is further confirmed by the fact that if we increase the Cs^+ concentration (at the same pH = 3), the proton reduction current is even lower (Fig. E.2 in Appendix E). In CO_2 atmosphere, the reduction current increases more significantly in the presence of 280 µM Cs^+ while almost no increase is observed in pure H_2SO_4. In Fig. 8.1b, we show that in the absence of Cs^+ no CO is detected in the anodic scan and the only current observed is due to charging of the electrical double layer, which nearly overlaps for both gaseous atmospheres. With Cs^+ in the electrolyte a large anodic current due to the oxidation of the CO produced is observed. Differently from CO_2 reduction, CO oxidation does take place in the absence of a metal ion in the electrolyte, as is seen in the control experiment (Fig. E.3 in Appendix E). To further confirm that Cs^+ is crucial for enabling the CO_2 reduction reaction, which causes the CO oxidation current observed, we have gradually added different amounts of Cs^+ ions to the electrolyte (Fig. E.4 in Appendix E). The amount of CO produced increases as a function of the Cs^+
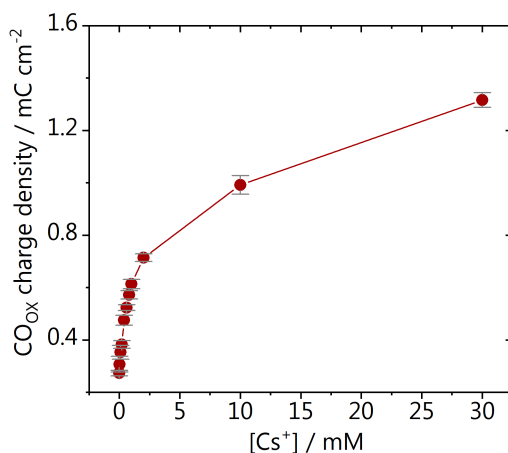
Fig. 8.2. Effect of the Cs$^+$ concentration. CO produced after polarization to −1 V vs. RHE, in the presence of different concentrations of Cs$^+$ in a Li$_2$SO$_4$ background electrolyte. The total cation concentration in solution was kept 0.1 M and the pH = 3. Error bars are calculated based on three individual measurements.
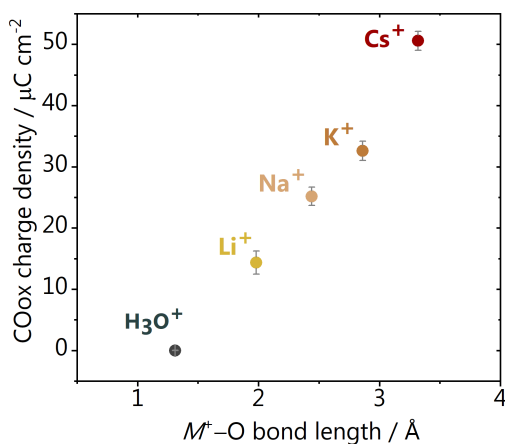

Fig. 8.3. Effect of the cation identity. CO detected on the gold sample directly after CO$_2$ reduction from 0 to −1.2 V vs. RHE in 1 mM M$_2$SO$_4$ with M = H, Li, Na, K, Cs. All solutions, when necessary, were adjusted to pH = 3. The M^+–O bond length is taken as the first peak of the cation-water radial distribution functions calculated from AIMD data, Table E.1 in Appendix E, whilst in the absence of a metal cation we used the proton-oxygen bond length.[28] Error bars are calculated based on three individual measurements.

concentration in the electrolyte, as derived from the CO oxidation currents from the CVs. Three subsequent CVs were recorded for every concentration and the trend remains the same over the different cycles.

This enhancement in the CO production by the addition of Cs^+ ions was investigated in a broader concentration range using Li_2SO_4 as background electrolyte at pH = 3. Here, the total cation concentration is kept constant (0.1 M) to avoid contributions of having solutions of different ionic strengths. The gold electrode was cycled from 0 to –1 V vs. RHE in the different electrolytes and the CO produced is oxidized in the positive-going scan, similarly to previous experiments (Fig. 8.1). The cyclic voltammetry is presented in Fig. E.5 in Appendix E and the charge of the CO oxidation peak found for the different concentrations of Cs^+ is depicted in Fig. 8.2. Already with the addition of less than 1 mM of Cs^+ to the electrolyte a steep increase in the CO production is observed. At higher concentrations, a saturation effect appears as the CO production approximates to a plateau.

We have also used the cathodic/anodic voltammetry during CO_2 reduction on gold to evaluate different metal cations in the dilute electrolytes used in this work. The gold electrode was flame annealed and characterized before each measurement and the blank voltammograms can be seen in Fig. E.1 in Appendix E. Experiments were performed in 1 mM M_2SO_4 where M = H, Li, Na, K, Cs. All solutions, if necessary, were adjusted to pH = 3, to exclude pH effects. Fig. 8.3 shows the CO oxidation charge of the first anodic cycle recorded after performing CO_2 reduction from 0 to –1.2 V vs. RHE. The activity for CO formation is correlated with the size of the solvated cation, here represented by the cation-oxygen ($M^+–H_2O$) bond length. Bond length for each alkali metal is taken as the first peak of cation-water radial distribution functions calculated from AIMD data (Table E.1 in Appendix E) and for the cation-free electrolyte, the proton-oxygen ($H^+–H_2O$) bond length is used.[28] In agreement with the previous results, no CO_2 reduction product is observed in the absence of a metal cation while in the M_2SO_4 electrolytes the activity for CO production follows the usual trend reported for other metal surfaces: Cs^+ > K^+ > Na^+ > Li^+.[3] We observe a strong correlation between activity and the cation size, which is related to a softer hydration shell, thus favoring the production of CO, in the Computational Model section.

8.3 Scanning Electrochemical Microscopy (SECM)

To confirm that in the absence of a metal cation absolutely no CO is produced on gold and to extend the study to silver and copper, relevant CO$_2$RR catalysts which are not good for CO oxidation, we have employed Scanning Electrochemical Microscopy (SECM) in the SG-TC mode to detect CO$_2$ reduction to CO. A schematic representation of the experiments is shown in Fig. 8.4a, where a platinum ultramicroelectrode (Pt-UME) is placed in the diffusion layer above the substrate electrode where CO$_2$ reduction takes place. The platinum voltammetry is extremely sensitive to trace amounts of CO, as CO strongly chemisorbs on the surface and can be removed by oxidation.[29] Platinum is also a suitable catalyst for hydrogen oxidation, thus we can also detect hydrogen produced due to HER. SECM was used here because of the higher sensitivity that it provides to detect CO, in comparison with other product analysis techniques such as Gas Chromatography (GC) and Differential Electrochemical Mass Spectrometry (DEMS). The procedure used for all measurements is shown in Fig. 8.4b. A negative potential is applied to the sample for 10 seconds and subsequently a cyclic voltammogram of the Pt–UME is recorded. Special care was taken with the samples and electrolytes used in these experiments, to make sure traces of metal impurities would not mislead our conclusions. The Pt-UME was prepared and characterized before each measurement. A blank voltammogram of the Pt-UME can be seen in Fig. 8.4c showing the expected voltammetric features of a clean polycrystalline platinum surface.[30] The polycrystalline gold, copper and silver samples used were also characterized before the measurements as shown in Fig. 8.4d, Fig. 8.4e and Fig. 8.4f, respectively. The voltammetry of copper and silver electrodes used for CO$_2$RR studies is rarely shown in literature, despite its importance to determine the quality of the surface preparation and consequently reproducibility of the experiments. Here, silver was characterized through the reversible Tl(I) underpotential deposition (UPD), which is used to assess the surface cleanliness and crystallinity.[31] This is seen by the presence and reversibility of the peaks from Fig. 8.4e. To evaluate the copper sample, the electrode was characterized in concentrated hydroxide solution, and the current due to the adsorption and desorption of OH$^-$ can be observed in the region of Cu$_2$O formation, also indicating the surface crystallinity.[32]
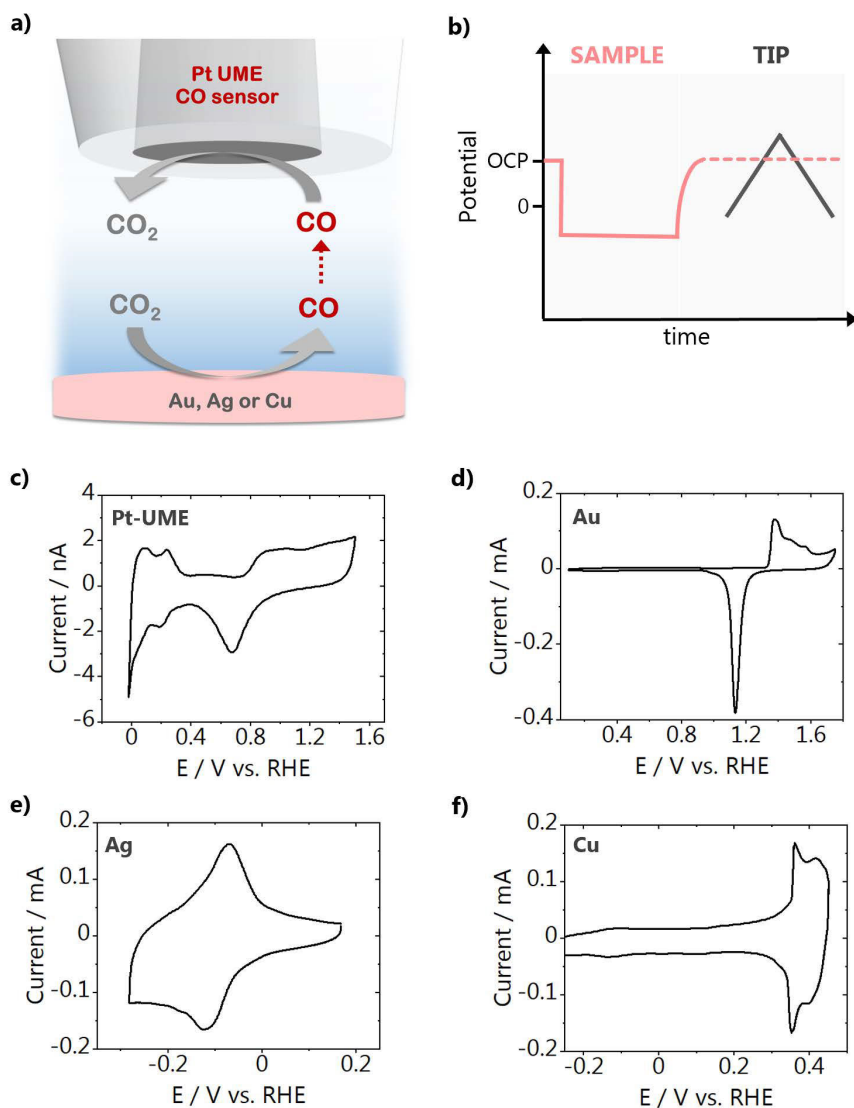
8

Fig. 8.4. SECM measurement scheme and characterization of the electrodes used. **a)** Schematic representation of the SECM experiment and **b)** method used to perform the measurements; **c)** Blank voltammetry of the Pt–UME used to perform the experiments taken in 0.1 M H_2SO_4; Characterization of: **d)** the gold sample in 0.1 M H_2SO_4; **e)** the silver sample through Tl(I) under potential deposition in 0.5 M Na_2SO_4 + 0.1 M H_2SO_4 + 0.1 M Tl_2SO_4; **f)** the copper sample in 0.5 M NaOH. All sample characterization CVs were recorded at 50 mV s^{-1}.
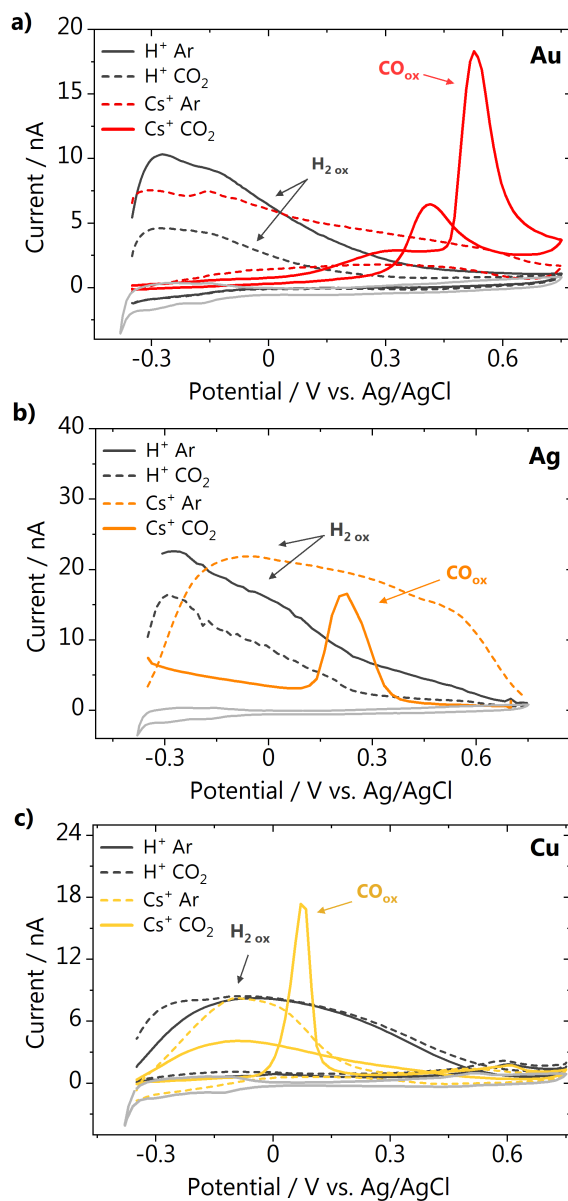
Fig. 8.5. CO detection with SECM. Cyclic voltammetry of the Pt–UME taken directly after CO_2 reduction on **a)** gold, **b)** silver and **c)** copper electrodes. The voltammetry of the Pt–UME before applying any potential to the sample is shown in light gray for reference.

The SECM measurements were carried out in 1 mM H_2SO_4 with and without the addition of 280 µM Cs^+. For each electrolyte, before CO_2 reduction, a control experiment in argon was performed, where only hydrogen is expected as a product. The Pt-UME was always positioned 50 ± 2 µm from the surface by performing a capacitive approach in air, which is essential for keeping the electrolyte free from impurities.[33–35] The uncertainty in the position is the error from the approach curve fits. Approach curves are reported in Fig. E.6 in Appendix E. Fig. 8.5a shows the results obtained for the gold electrode after applying a potential of –0.7 V vs. RHE to the sample. In argon atmosphere, in the absence or presence of Cs^+ only current characteristic to hydrogen oxidation can be seen in the Pt-UME voltammetry. In CO_2 atmosphere, only when Cs^+ is added to the electrolyte a sharp peak due to the oxidation of CO is seen, which confirms that CO_2 reduction on gold does not take place in the absence of a metal cation in solution. Fig. 8.5b shows similar results for the silver electrode at a potential of –0.8 V vs. RHE. As for gold, on silver CO_2 reduction takes place only in the Cs^+ containing electrolyte, as confirmed by the CO oxidation peak in the Pt–UME voltammetry. On copper the same trend is observed when the sample is polarized at –1 V vs. RHE (Fig. 8.5c). In the 1 mM H_2SO_4 electrolyte only hydrogen is detected by the Pt-UME, whilst CO is detected only after addition of Cs^+ to the electrolyte. It must be noted that these individual SECM measurements constitute only a qualitative tool to probe if CO is formed or not. Due to various factors as the different sample potentials applied, bubble formation, diffusion hindrance by the tip, the magnitude of the CO and H_2 oxidation currents measured and their potentials cannot be used for a quantitative comparison between the substrates. For silver and copper, the potential range applicable is limited by the stability of the electrode. At more cathodic potentials, a small amount of metal oxide dissolution is observed and the traces of Ag^+ and Cu^{2+} ions released into the electrolyte lead to the production of CO in 1 mM H_2SO_4 (see Section E.3.2 in Appendix E for details).[36] This happens as during the SECM approach, the electrode surface is exposed to air, which can lead to the formation of (a very small amount) of oxide on the surface. This is confirmed by the Pt-UME voltammetry (Fig. E.7 in Appendix E), which presents voltammetric features characteristic of the under potential deposition of Ag^+ or Cu^{2+} on the Pt-UME surface.[37,38]

8.4 Computational model

To model the experimental system, we carried out DFT-based *ab initio* molecular dynamics on a $3\sqrt{3}\times3\sqrt{3}$–$R30°$ Au(111) supercell (4 layers, 15.3 Å × 15.3

Å × 30.0 Å) with 72 explicit water molecules filling 15.0 Å along Z, plus 8 Å vacuum thickness between periodic slabs (see Fig. E.8 in Appendix E, and Videos 1-5 in the online version of the publication).[39] This pristine system (Au–H₂O) is equilibrated for 2 ps at 300 K with a time step of 1 fs, as illustrated in Fig. 8.6a. Then, an alkali metal cation M^+ (M = Li, Na, K, Cs) is inserted close to the gold surface, at an initial cation-surface distance of 3.3 Å. Upon optimization, the cation-surface distances increase for each alkali metal (Fig. E.9 in Appendix E). To specifically investigate the local interactions between cation and CO₂, we kept the cation concentration at the OHP constant, balancing the charge within the unit cell by including an OH⁻ at the fourth water bilayer (see Methods in Appendix E). Given the volume of the solvation layer and the number of water molecules, the cation surface coverage (0.04 ML) corresponds to a concentration around 0.5–0.8 M. Since the initial position and surface coverage are identical for each cation, any concentration effects are not included in the model. We let the cation solvation shell build up for 2 ps and we classify the final structures as Au-H₂O-M^+ (Fig. 8.6a). The resulting cation-oxygen radial distribution functions $g_{M+\text{-H2O}}(r)$ (Eq. E.6 and E.7, Fig. E.10) confirmed a proper description of the cation coordination shell, since the estimated cation-oxygen distances $d_{M+\text{-O}}$ for water molecules in the first solvation shell agree with previous experimental and theoretical results (Table E.1 in Appendix E). Furthermore, the full width at half maximum (FWHM) for the first $g_{M+\text{-H2O}}(r)$ peak increases following the alkali group, Li⁺ < Na⁺ < K⁺ < Cs⁺, thus confirming that a larger cation ionic radius implies a softer solvation shell. Finally, we estimate the cation coordination numbers through the structural parameters previously defined (Eq. E8 and E9 in Appendix E). The alkali cations exhibit an average coordination number of 2.8, 3.2, 3.5, and 5.8, with maximum values of 3.9, 4.7, 4.9, and 8.0 for Li⁺, Na⁺, K⁺, and Cs⁺ respectively, in line with state-of-the-art reported values (see Table E.2 in Appendix E).[40]

After the equilibration of the Au-H₂O-M^+ systems, we introduce a CO₂ molecule at the electrolyte/surface interface in the proximity of the solvated cation (Fig. 8.6a). Upon AIMD simulations for 2 additional ps, CO₂ adsorbs on the gold surface in a $\eta^2_{C,O}$ conformation (bidentate through the carbon atom and one oxygen) and coordinates to the surrounding cation and water molecules through the second oxygen. Due to its hard solvation shell, Li⁺ coordinates to CO₂ for limited periods of the AIMD runs, resulting in an average coordination number $N_{Li+\text{−O(CO2)}}$ of 0.1 ± 0.3 (Fig. 8.6b, Table E.2 in Appendix E). Instead, other alkali metals continuously bind to the oxygen atom in CO₂, herein called O(CO₂), resulting in the
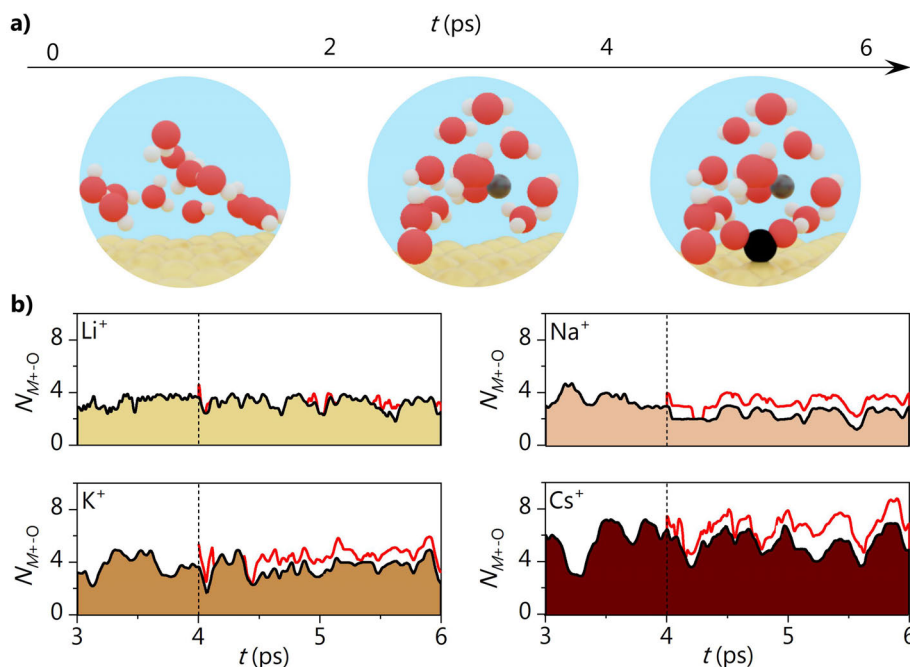
Fig. 8.6. Cation coordination with CO_2. **a)** Timeline for the *ab initio* molecular dynamics simulation at 300 K: 2 ps pre-equilibration for the Au-H_2O system, 2 ps for the Au-H_2O-M^+ system (cation inserted close to the surface, ϑ_{M+} = 0.04 ML), and finally 2 ps for the Au-H_2O-M^+-CO_2 system (CO_2 molecule adsorbed on Au). The portrayed cation is Li^+. **b)** Alkali cation's coordination number, N_{M+-O}, vs. simulation time for the Au-H_2O-M^+ system. Dashed lines indicate CO_2 insertion in the supercell (t = 4 ps) and red continuous lines indicate the increase in coordination number due to M^+–$O(CO_2)$.

following coordination numbers: $N_{Na+-O(CO2)}$ = 0.9 ±0.2, $N_{K+-O(CO2)}$ = 0.9 ± 0.4, and $N_{Cs+-O(CO2)}$ = 1.3 ± 0.5. Upon coordination to M^+–$O(CO_2)$, the number of water molecules within the cation´s coordination shell remains constant or slightly decreases (Fig. 8.6b).

Partially desolvated cations have three promotional effects which enable CO_2 reduction. The first effect is thermodynamic (Fig. 8.7a). When the cation coordinates to the adsorbate, a short-range M^+–O (CO_2) electrostatic interaction stabilizes CO_2 more strongly than the solvation by water molecules alone by around 0.5 eV (Fig. 8.7a, Table E.3 and Eq. E.8 in Appendix E). Besides, there is a medium-range interaction between the electric dipole of adsorbed *CO_2^- and a cation-induced
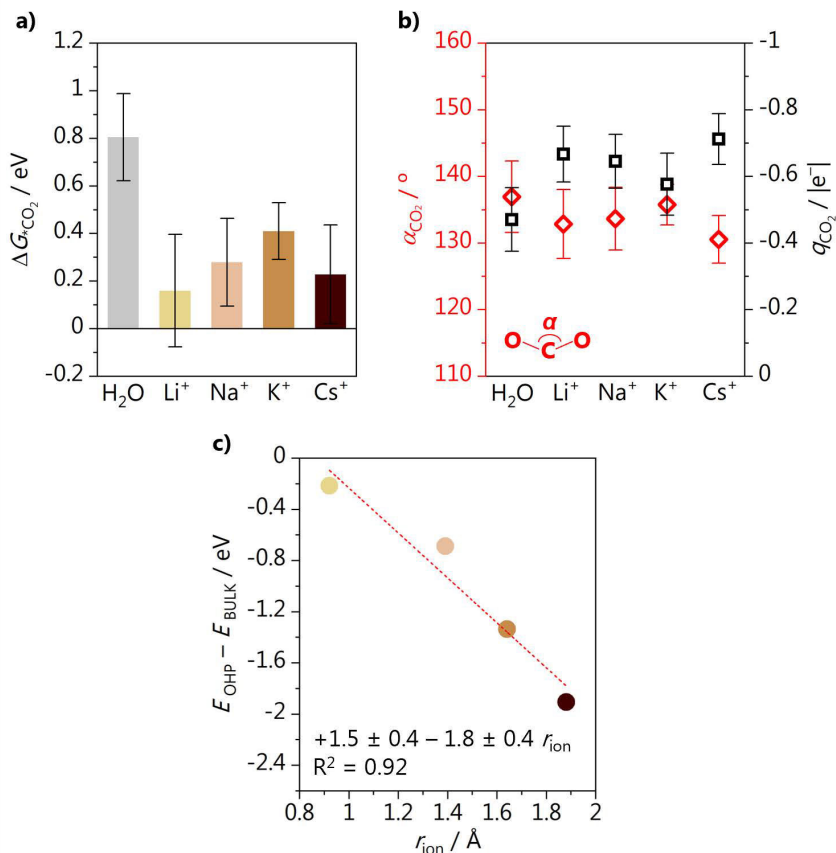
Fig. 8.7. CO_2 activation *via* explicit cation/intermediate interaction, driven by cation concentration at the OHP. **a)** Average CO_2 adsorption Gibbs free energy at $U = 0$ V vs SHE in absence (gray) or presence of an alkali cation (light to dark brown), with CO_2 and environment (Au-H_2O or Au-H_2O-M^+) as energy references. **b)** CO_2 activation angle, α, and CO_2 Bader charge, q_{CO_2}, are shown in red and black, respectively, and reported in Table E.4 in Appendix E. Error bars are calculated as standard deviation of the data (see Methods). **c)** Correlation between thermodynamic driving force at $U = 0$ V vs SHE for different alkali cations to accumulate at the outer Helmholtz plane (OHP) and their ionic radius (see Methods). Coefficients $a = 1.5 \pm 0.4$ eV; $b = 1.5 \pm 0.8$ eV Å^{-1}.
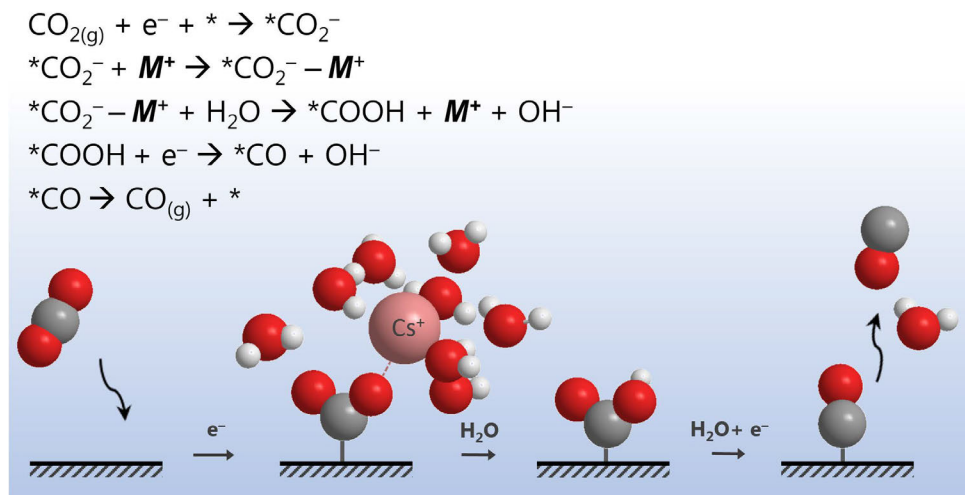
$$CO_{2(g)} + e^- + * \rightarrow *CO_2^-$$
$$*CO_2^- + \boldsymbol{M^+} \rightarrow *CO_2^- - \boldsymbol{M^+}$$
$$*CO_2^- - \boldsymbol{M^+} + H_2O \rightarrow *COOH + \boldsymbol{M^+} + OH^-$$
$$*COOH + e^- \rightarrow *CO + OH^-$$
$$*CO \rightarrow CO_{(g)} + *$$

Fig. 8.8. Mechanism of CO_2 reduction to CO. Schematic representation of the interaction of the cation with the negatively charged CO_2^- intermediate together with a proposed reaction mechanism.

electric field, which is irregular and modulated by the electrolyte, solvation and neighboring cations (see Eq. E10 and E11 and Fig. E.11 in Appendix E). [22,27]

Both short and medium-range cation-induced interactions account for an equivalent stabilizing effect. Instead, in the absence of cations, the medium-range $*CO_2^-$-dipole/electric field interaction only accounts for weaker stabilization (–0.2 eV), unable to open the CO_2 reduction pathway (see Eq. E.12 and Fig. E.12 in Appendix E). The second promotional effect is the O–C–O angle α activation, which decreases from linear 180° to below 140° in the presence of a neighboring cation (Fig. 8.7b, red axis, Table E.4 in Appendix E). Thirdly, upon coordination, cations enhance the electron transfer from the catalytic surface to the CO_2 unit, as demonstrated by the CO_2 Bader charges close to –1.0 $|e^-|$ (Fig. 8.7c, Table E.4 in Appendix E). Thus, partially desolvated cations are crucial for the formation of the CO_2^- intermediate, the generally assumed rate-determining step for CO_2 reduction.[41] As a final remark, the activity trends based solely on cation radius (Fig. 8.3) originate both from different cation surface concentrations at the OHP (Fig. 8.7c, Eq. E.8-12 in Appendix E)[27] and their different ability to coordinate to $*CO_2^-$, which ranges from almost no bond for Li^+ to more than a bond for Cs^+, Table E.2.

8.5 Discussion and Conclusions

The results presented here show that without a metal cation in the electrolyte, CO$_2$ reduction to CO does not take place, neither on gold, silver, or copper electrodes. As discussed earlier, there are currently three major theories regarding the main role of metal cations during CO$_2$ reduction: modification of the (local) electric field, buffering of the interfacial pH and stabilization of reaction intermediates via local field effects. All theories have been supported with experiments and DFT models, and to some extent they all play a role on the CO$_2$ reduction reaction. However, based on our experimental and theoretical results, we rule out that the modification of the local electric field or buffering of the local pH are the main reasons for the cation effects observed. These theories suggest that the cation should just affect the CO$_2$ reduction rate and that this reaction should still take place in cation-free electrolytes. Our results also confirm the view suggested by Chen et al.[22] and Resasco et al.[27], i.e. that a key role of cations on CO$_2$ reduction is to stabilize negatively charged reaction intermediates, such as *CO$_2^-$ and *OCCO$^-$ via a local electric field effect. Besides the medium-range electric field/electric dipole interaction, we show here an explicit short-range local electrostatic interaction between partially desolvated metal cation and CO$_2$ accounting for a similar stabilization. Fig. 8.8 shows our proposed reaction mechanism based on the discussed experimental and computational results, together with a pictorial representation. Here, we suggest that the cation is the crucial promoter to enable the reduction process, by forming a complex with CO$_2$ which allows the formation of the CO$_2^-$ intermediate. Additionally, as shown in Fig. 8.2, the more Cs$^+$ is added to the electrolyte, the more CO is produced, similarly to ethylene formation on copper, which follows the cation radius trend: Cs$^+$ > K$^+$ > Na$^+$ [27]. We propose that the differences in activity observed among the alkali cations for CO$_2$ reduction are correlated with their different concentrations at the OHP (Fig. 8.7c) and their different capability of interacting with negatively charged adsorbates, as indicated by significantly different cation-CO$_2$ average coordination numbers over the 2 ps simulation time (Fig. 8.6b). Metal cations with a softer hydration shell have a higher concentration at the interface and they show a stable coordination with CO$_2$ (Na$^+$, K$^+$, Cs$^+$, Fig. 8.6b), thus they are more likely to stabilize it via a M^+–O(CO$_2$) local interaction. Instead, hard shell cations as Li$^+$ coordinate poorly with CO$_2$, thus they are less effective in enabling this stabilization effect.

The knowledge that CO_2 can only be reduced in the presence of a metal cation interacting with the CO_2^- intermediate, has important implications. From the system design point-of-view, research efforts should focus on finding species that might have an even larger stabilizing effect on CO_2 than Cs^+, such as large multivalent cations[42] or surfactants[7]. Additionally, from the reaction modeling point-of-view, our results highlight that an accurate understanding of the electrochemical activation of CO_2 on copper, silver, and gold must involve cations and water. To simply assume a proton-coupled electron transfer as a first step in DFT-based electrocatalysis fails to account for the stabilization of the key reaction intermediates by electrolyte cations.[43–45] Instead, we here show that the explicit inclusion of cationic species allows the stabilization of the CO_2^- intermediate by around 0.5 eV and is needed to properly estimate its energy. Finally, our mechanism suggests that, at least for a pH of 3 or higher, water is the relevant hydrogen/proton donor, rather than hydronium itself which cannot activate CO_2. As a result, the CO_2 reduction reaction does not consume protons, but it generates OH^-. This statement agrees with, and provides an explanation for, our recent observation that in mildly acidic media, CO_2 reduction can completely suppress the proton reduction to hydrogen, by neutralizing protons through the generated OH^-, rendering the protons no longer available for hydrogen formation.[46]

References

(1)   Kortlever, R.; Shen, J.; Schouten, K. J. P.; Calle-Vallejo, F.; Koper, M. T. M. *J. Phys. Chem. Lett.* 2015, *6* (20), 4073–4082.

(2)   König, M.; Vaes, J.; Klemm, E.; Pant, D. *iScience* 2019, *19*, 135–160.

(3)   Moura de Salles Pupo, M.; Kortlever, R. *ChemPhysChem* 2019, *20* (22), 2926–2935.

(4)   Setterfield-Price, B. M.; Dryfe, R. A. W. *J. Electroanal. Chem.* 2014, *730*, 48–58.

(5)   Verma, S.; Lu, X.; Ma, S.; Masel, R. I.; Kenis, P. J. A. *Phys. Chem. Chem. Phys.* 2016, *18* (10), 7075–7084.

(6)   Thorson, M. R.; Siil, K. I.; Kenis, P. J. A. *J. Electrochem. Soc.* 2012, *160* (1), F69–F74.

(7)   Banerjee, S.; Zhang, Z.; Hall, A. S.; Thoi, V. S. *ACS Catal.* 2020, *10* (17), 9907–9914.

(8)   Zhang, Q.; Shao, X.; Yi, J.; Liu, Y.; Zhang, J. *Chinese J. Chem. Eng.* 2020, *28* (10), 2549–2554.

(9)   Shen, J.; Lan, D.; Yang, T. *Int. J. Electrochem. Sci.* 2018, *13* (10), 9847–9857.

(10)   Kyriacou, G. Z.; Anagnostopoulos, A. K. *J. Appl. Electrochem.* 1993, *23*, 483–486.

(11)   Kim, H.; Park, H. S.; Hwang, Y. J.; Min, B. K. *J. Phys. Chem. C* 2017, *121* (41), 22637–22643.

(12)   Kim, H.-Y.; Choi, I.; Ahn, S. H.; Hwang, S. J.; Yoo, S. J.; Han, J.; Kim, J.; Park, H.; Jang, J. H.; Kim, S.-K. *Int. J. Hydrogen Energy* 2014, *39* (29), 16506–16512.

(13)   Gunathunge, C. M.; Ovalle, V. J.; Waegele, M. M. *Phys. Chem. Chem. Phys.* 2017, *19* (44), 30166–30172.

(14)   Waegele, M. M.; Gunathunge, C. M.; Li, J.; Li, X. *J. Chem. Phys.* 2019, *151* (16), 160902.

(15)   Akhade, S. A.; McCrum, I. T.; Janik, M. J. *J. Electrochem. Soc.* 2016, *163* (6), F477–F484.

(16)   Strmcnik, D.; van der Vliet, D. F.; Chang, K.-C.; Komanicky, V.; Kodama, K.; You, H.; Stamenkovic, V. R.; Marković, N. M. *J. Phys. Chem. Lett.* 2011, *2* (21), 2733–2736.

(17)   Strmcnik, D.; Kodama, K.; Van Der Vliet, D.; Greeley, J.; Stamenkovic, V. R.; Marković, N. M. *Nat. Chem.* 2009, *1* (6), 466–472.

(18)   Murata, A.; Hori, Y. *Bull. Chem. Soc. Jpn.* 1991, *64* (1), 123–127.

(19)   Hori, Y.; Suzuki, S. *Bull. Chem. Soc. Jpn.* 1982, *55* (3), 660–665.

(20)   Frumkin, A. N. *Trans. Faraday Soc.* 1959, *55* (1), 156–167.

(21)   Ringe, S.; Clark, E. L.; Resasco, J.; Walton, A.; Seger, B.; Bell, A. T.; Chan, K. *Energy Environ. Sci.* 2019, *12* (10), 3001–3014.

(22)   Chen, L. D.; Urushihara, M.; Chan, K.; Nørskov, J. K. *ACS Catal.* 2016, *6* (10), 7133–7139.

(23)   Hussain, G.; Pérez-Martínez, L.; Le, J.-B.; Papasizza, M.; Cabello, G.; Cheng, J.; Cuesta, A. *Electrochim. Acta* 2019, *327*, 135055.

(24)   Singh, M. R.; Kwon, Y.; Lum, Y.; Ager, J. W.; Bell, A. T. *J. Am. Chem. Soc.* 2016, *138* (39), 13006–13012.

(25)   Ayemoba, O.; Cuesta, A. *ACS Appl. Mater. Interfaces* 2017, *9* (33), 27377–27382.

(26)   Zhang, F.; Co, A. C. *Angew. Chemie - Int. Ed.* 2020, *59* (4), 1674–1681.

(27)   Resasco, J.; Chen, L. D.; Clark, E.; Tsai, C.; Hahn, C.; Jaramillo, T. F.; Chan, K.; Bell, A. T. *J. Am. Chem. Soc.* 2017, *139* (32), 11277–11287.

(28)   Silvestrelli, P. L. *J. Chem. Phys.* 2017, *146* (24), 1–31.

(29)   García, G.; Koper, M. T. M. *ChemPhysChem* 2011, *12* (11), 2064–2072.

(30)   Jacobse, L.; Raaijman, S. J.; Koper, M. T. M. *Phys. Chem. Chem. Phys.* 2016, *18* (41), 28451–28457.

(31)   Bewick, A.; Thomas, B. *J. Electroanal. Chem.* 1975, *65* (2), 911–931.

(32)   Schouten, K. J. P.; Pérez-Gallent, E.; Koper, M. T. M. *J. Electroanal. Chem.* 2013, *699*, 6–9.

8

(33)   Monteiro, M. C. O.; Jacobse, L.; Touzalin, T.; Koper, M. T. M. *Anal. Chem.* 2020, *92* (2), 2237–2243.

(34)   Voogd, J. M. De; Spronsen, M. A. Van; Kalff, F. E.; Bryant, B.; Ostoji, O.; Haan, A. M. J. Den; Groot, I. M. N.; Oosterkamp, T. H.; Otte, A. F.; Rost, M. J. *Ultramicroscopy* 2017, *181*, 61–69.

(35)   Monteiro, M. C. O.; Jacobse, L.; Koper, M. T. M. *J. Phys. Chem. Lett.* 2020, *11* (22), 9708–9713.

(36)   Henckel, D. A.; Counihan, M. J.; Holmes, H. E.; Chen, X.; Nwabara, U. O.; Verma, S.; Rodríguez-López, J.; Kenis, P. J. A.; Gewirth, A. A. *ACS Catal.* 2021, *11* (1), 255–263.

(37)   Lukaszewski, M.; Soszko, M.; Czerwiński, A. *Int. J. Electrochem. Sci.* 2016, *11* (6), 4442–4469.

(38)   Macao, L. H.; Santos, M. C.; Machado, S. A. S.; Avaca, L. A. *J. Chem. Soc. - Faraday Trans.* 1997, *93* (22), 3999–4003.

(39)   Bellarosa, L.; García-Muelas, R.; Revilla-López, G.; López, N. *ACS Cent. Sci.* 2016, *2* (2), 109–116.

(40)   Marcus, Y. *Chem. Rev.* 2009, *109*, 1346–1370.

(41)   Birdja, Y. Y.; Pérez-Gallent, E.; Figueiredo, M. C.; Göttle, A. J.; Calle-Vallejo, F.; Koper, M. T. M. *Nat. Energy* 2019, *4* (9), 732–745.

(42)   Schizodimou, A.; Kyriacou, G. *Electrochim. Acta* 2012, *78*, 171–176.

(43)   Nørskov, J. K.; Rossmeisl, J.; Logadottir, A.; Lindqvist, L.; Kitchin, J. R.; Bligaard, T.; Jónsson, H. *J. Phys. Chem. B* 2004, *108* (46), 17886–17892.

(44)   Peterson, A. A.; Abild-Pedersen, F.; Studt, F.; Rossmeisl, J.; Nørskov, J. K. *Energy Environ. Sci.* 2010, *3*, 1311–1315.

(45)   Rossmeisl, J.; Chan, K.; Ahmed, R.; Tripković, V.; Björketun, M. E. *Phys. Chem. Chem. Phys.* 2013, *15*, 10321–10325.

(46)   Bondue, C. J.; Graf, M.; Goyal, A.; Koper, M. T. M. *J. Am. Chem. Soc.* 2021, *143* (1), 279–285.

8